Check for updates

View Article Online
View Journal

PCCP
Physical Chemistry Chemical Physics

Accepted Manuscript

This article can be cited before page numbers have been issued, to do this please use: M. F. Gromboni, P. J. M. Cordeiro-Junior, P. Corradini, L. H. Mascaro and M. R. D. V. Lanza, *Phys. Chem. Chem. Phys.*, 2022, DOI: 10.1039/D2CP00072E.

Volume 19
Number 1
7 January 2017
Pages 1-896

PCCP
Physical Chemistry Chemical Physics
rsc.li/pccp

ISSN 1463-9076

ROYAL SOCIETY OF CHEMISTRY

PAPER
H.-P. Loock *et al.*
Determination of the thermal, oxidative and photochemical degradation rates of scintillator liquid by fluorescence EEM spectroscopy

This is an Accepted Manuscript, which has been through the Royal Society of Chemistry peer review process and has been accepted for publication.

Accepted Manuscripts are published online shortly after acceptance, before technical editing, formatting and proof reading. Using this free service, authors can make their results available to the community, in citable form, before we publish the edited article. We will replace this Accepted Manuscript with the edited and formatted Advance Article as soon as it is available.

You can find more information about Accepted Manuscripts in the Information for Authors.

Please note that technical editing may introduce minor changes to the text and/or graphics, which may alter content. The journal's standard Terms & Conditions and the Ethical guidelines still apply. In no event shall the Royal Society of Chemistry be held responsible for any errors or omissions in this Accepted Manuscript or any consequences arising from the use of any information it contains.

ROYAL SOCIETY OF CHEMISTRY

rsc.li/pccp

View Article Online
DOI: 10.1039/D2CP00072E

ARTICLE

One-step preparation of $Co_2V_2O_7$: synthesis and application as Fenton-like catalyst in gas diffusion electrode

Received 00th January 20xx,
Accepted 00th January 20xx

DOI: 10.1039/x0xx00000x

Murilo Fernando Gromboni[a]†*, Paulo Jorge Marques Cordeiro-Junior[a]†, Patricia Gon Corradini[b,c], Lucia Helena Mascaro[b], Marcos Roberto de Vasconcelos Lanza[a*]

Bimetallic oxides and MOFs have been employed as catalysts for ORR via two-electron and Fenton-based processes. This work reports the development of a new green one-step route for obtaining $Co_2V_2O_7$. The $Co_2V_2O_7$ oxide was immobilized on Printex-L6 carbon and used as catalyst for oxygen reduction reaction (ORR) and in heterogeneous Fenton-based processes. The PL6C/2.5% $Co_2V_2O_7$ sample exhibited the best performance in ORR via two-electron pathway, increasing the selectivity for H_2O_2 generation. Electrochemical impedance spectroscopy analysis showed a decrease in charge transfer resistance in the $Co_2V_2O_7$/PL6C matrix. The application of gas diffusion electrode (GDE) modified with 2.5% $Co_2V_2O_7$ resulted in 30% increase in H_2O_2 production compared to the unmodified GDE. The unmodified GDE promoted methyl-paraben (MeP) removal of ~80% after 90 min treatment, whereas the modified GDE promoted ~90% of MeP removal in 30 min. The results obtained point to the potential of $Co_2V_2O_7$ in improving the efficiency of GDE when applied for the treatment of organic pollutants.

Introduction

Water is a scarce natural resource, and despite the fact that it covers a large proportion of the Earth surface, only a small portion of this natural resource is available for human consumption. Unfortunately, this small portion of water available for human consumption is not equally distributed among the countries in the world. Moreover, the little water available for use is increasingly compromised by pollution. Thus, in view of its prevalent scarcity, it is essentially crucial to develop new, affordable and efficient mechanisms for the treatment of water intended for human consumption. One of the major classes of water contaminants are the persistent organic pollutants (POPs); these emerging pollutants can be efficiently removed from water through advanced oxidation processes (AOP). AOPs are a low-cost environmentally friendly alternative mechanism used as a complement to the classical methods for the treatment of water. Advanced oxidation processes (AOPs) involve the use of strong oxidants, such as hydroxyl radicals ($^{\cdot}OH$), to mineralize/convert POPs into CO_2, H_2O, and inorganic ions[1, 2].

Generally, some AOPs operate through the activation of H_2O_2 which can be mediated by Fe(II) (H_2O_2/Fe^{2+} - the Fenton method), by UV light (H_2O_2/UV), or by a combination of the Fenton method and UV light (H_2O_2/Fe^{2+}/UV)[3]. In spite of being simple to perform, traditional AOPs have some underlying limitations. These traditional processes tend to maintain the concentration of H_2O_2 constant during the degradation process; in addition, the processes also require extreme care and high costs of H_2O_2 storage and transport[4]. In view of that, electrochemical advanced oxidation processes (EAOP) have been developed with the aim of circumventing the aforementioned limitations of AOPs through the *in situ* production of H_2O_2 by oxygen reaction reduction (ORR) via two-electron pathway, rather than via four-electron mechanism [5], as can be observed in equations (1) and (2) below:

$$O_2 + 2H^+ + 2e^- \rightarrow H_2O_2 \qquad (1)$$

$$O_2 + 4H^+ + 4e^- \rightarrow 2H_2O \qquad (2)$$

One of the EAOPs applied *via* ORR is the electro-Fenton process (EF); this technique is based on the Fenton method where hydrogen peroxide (H_2O_2) is produced at the cathode [6], thus promoting a continuous controlled production of H_2O_2[2].

Bidimensional electrodes constructed using carbonaceous materials (CMs) can be used as cathodes for the reduction of O_2 dissolved in aqueous matrices since these materials exhibit good selectivity for the reaction via the two-electron pathway and have a high rate of O_2 adsorption [1, 7, 8]. However, the efficiency of carbon-based bidimensional electrodes is limited when it comes to the generation of H_2O_2; this is due to the low concentration of O_2 dissolved in the medium[8]. In view of that, gas diffusion electrodes (GDEs) have been employed as alternative cathodes for the in situ production of H_2O_2; this is because GDEs have large surface area and do not present the kind of limitation associated with low quantity of oxygen dissolved in water, since O_2 is derived from the gas phase (air or pure O_2) in these electrodes [5].

---

[a] *São Carlos Institute of Chemistry, University of São Paulo, São Carlos, SP, Brazil*
[b] *Department of Chemistry, Federal University of São Carlos, São Carlos, SP, Brazil*
[c] *Fluminense Federal Institute of Education, Campus Itaperuna, Itaperuna,RJ ,Brazil*
† Both authors contributed equally to the development of this work
* Corresponding authors E-mail addresses: mgromboni@gmail.com (M.F. Gromboni); marcoslanza@usp.br (M. R. V. Lanza)

Electronic Supplementary Information (ESI) available to download. The original data are deposited in the dataset, see DOI: 10.17632/9hjfrjw76x.1.

View Article Online
DOI: 10.1039/D2CP00072E

A wide range of carbonaceous materials (CMs) have been used to modify GDEs in order to improve the performance of these electrodes; some of the CMs used as modifiers of GDEs have included carbon black[5, 9], N-doped carbon [10], and carbon felts[3]. One of these modifiers which has attracted considerable attention is Printex L6 carbon (PL6C); this carbon material is relatively less expensive and has been found to have good energetic efficiency[5, 11]. To help enhance the efficiency of carbon-modified GDEs, different electrocatalysts have also been incorporated into the CMs; some of the electrocatalysts employed have included organic compounds[5], oxides[9], nanoparticles[3], and metal-organic frameworks (MOFs)[12].

Oxide electrocatalysts can function via oxygen adsorption processes or by mediating the reduction process[9, 13-15]. Vanadium oxides have been studied for H_2O_2 electrogeneration [14, 16]. The incomplete d orbital of vanadium, present in V_2O_5, increases chemical surface interactions. Due to the voids between its biding, meaning enhanced reversible adsorption of oxygen into its cavities [16]. This means that several V_2O_5 molecules bond together to form the vanadyl radical, leading to an increase in defects and facilitating oxygen adsorption [14]. Cobalt oxides, on the other hand, are investigated because they alter the binding energies of •OOH, •O, and •OH[17, 18]. In the case of CoO_x, the ORR active sites have an ideal affinity for •OOH, resulting in a high selectivity for the two-electron pathway[17].

More recently, bimetallic oxides [19-21] have been employed as catalysts for ORR due to the fact that some transition metal oxides are reduced on the surface of the cathode during the process, generating metals with intermediate oxidation states (MIOS) which play an important role in ORR by mediating the electron transfer from the electrode to O_2 [13] and are found to promote the catalyzation of H_2O_2 generation due to their lower valence [9, 13]. In addition, the reduction of bimetallic metals increases the oxygen vacancies on the surface of the electrode, and this leads to greater oxygen mobility and higher electrogeneration of H_2O_2[21]. Interestingly, some previous studies reported in the literature have employed bimetallic MOFs as simultaneous catalysts for ORR and in Fenton-like processes; the use of these MOFs has been found to enhance H_2O_2 production while promoting the activation of H_2O_2 generated by photogenerated electron or by the electron supplied by the system[12, 22]. Very few studies reported in the literature have investigated the combined application of *in situ* production of H_2O_2 with heterogeneous catalysis on the cathode surface[23-29]; most of these studies employed catalysts that contained Fe(II)/Fe(III) in their analyses. Ganiyu *et al*.[26, 27] used a hierarchical CoFe-layered double hydroxide immobilized on carbon felt for heterogeneous electro-Fenton catalysis; here, the author employed Co(II) as co-catalyst for •OH generation. Another interesting work that deserves mentioning is that of Ghasemi *et al*.[28] who used CuFeN immobilized on carbon nanotubes for the degradation of cefazolin. In studies conducted by Liang *et al.*[23, 24], the authors used transition metals nanoparticles (Cu, Co, Mn, Ce) immobilized on gas diffuse electrode surface to improve the in-situ production of H_2O_2 while the valence sites of the metals, which operated as a Fenton-like heterogeneous catalyst, promoted H_2O_2 activation. More recently, Wu *et al.* [29] used gas diffusion electrode/boron-modified graphene aerogel for H_2O_2 generation where the Boron atoms mediated the activation of H_2O_2 producing •OH radicals in a wide range of pH (4-9). It is worth noting that, to date, there have been no reports in the literature regarding the simultaneous application of iron-free bimetallic oxides as hetereneous catalysts for ORR and for the activation of H_2O_2 generated in the system.

Previous studies reported in the literature have demonstrated the efficiency of cobalt oxides [15, 17] and vanadium oxides [16, 30] when applied toward the electrogeneration of H_2O_2. To the best of our knowledge, no studies have been reported regarding the combined application of mixed-metal oxide (cobalt vanadate - $Co_2V_2O_7$) for the electrogeneration of hydrogenperoxide. Quite recently, Zhang *et al.*[31] employed $Co_2V_2O_7$ as a peroxidase-like nanoenzyme for the catalyzation of H_2O_2 to form hydroxyl radical (•OH); the authors investigated the ability of $Co_2V_2O_7$ to mediate peroxide activation to oxidize benzoic acid. The study revealed that even at a low concentration (0.08 µM) of H_2O_2, $Co_2V_2O_7$ was able to promote the formation of •OH, demonstrating the ultra sensitivity of the material ($Co_2V_2O_7$) in this reaction. Also, Zhang *et al.* [31] showed that the application of $Co_2V_2O_7$ led to the generation of a small amount of H_2O_2 through heterogeneous catalysis from the reduction of oxygen dissolved in the solution on the surface of the dispersed powder.

In the present study, we describe the design of a one-step green route for the synthesis of the bimetallic oxide $Co_2V_2O_7$ in this paper. We also tested the bimetallic oxide's ability to mimic the known actions of the individual oxides of V[16] and Co[17], as well as its ability to activate the H_2O_2[31] generated in the modified carbonaceous matrix. The ORR process was evaluated by linear sweep voltammetry (LSV) based on the application of a porous microlayer technique on rotatory ring-disk electrode (RRDE) and electrochemical impedance spectroscopy (EIS). The modification of the GDE was performed using optimal conditions. In addition, the study sought to analyze the efficiency of the proposed PL6C/$Co_2V_2O_7$-GDE for the production of H_2O_2 and for the removal of methyl-paraben in residual water. The application of the proposed material for the removal of methyl-paraben was investigated with the aim of testing the potential use of the modifier ($Co_2V_2O_7$) as a Fenton-like catalyst[12, 31].

Results and discussion

Structure and composition analysis

Several techniques have been employed for the synthesis of $Co_2V_2O_7$; some of these techniques are solid-state reaction[32], sol-gel[33], solution precipitation[34], and hydrothermal synthesis [35]. In the present study, CoV_2O_7 was synthesized by the direct mixing of stoichimetrically dissolved amounts of Co(II) – acid solution, and V(V) – alkaline solution, dropwise. No surfactants, additives, or organic solvents were used in the proposed technique. The steps involved and the scheme illustrating the synthesis of the material (cobalt vanadate) are shown in Figure 1A. The material obtained was characterized as-synthesized without heat treatment. As can be seen in Figure 1B, the XRD patterns obtained showed that the synthesized material exhibited crystalline characteristics (crystallinity). All the peaks of the as-synthesized sample was assigned exclusively to the monoclinic $Co_2V_2O_7$ (PDF 01-070-1189), and no secondary phase was detected.

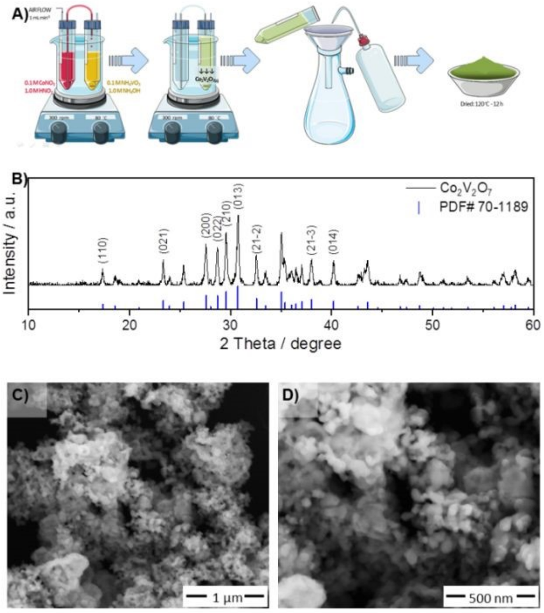

Figure 1. (A) Illustrative scheme of the drop by drop system and the steps involved in the synthesis of the material under the route employed. (B) Diffractogram of the as-synthesized sample and the XRD patterns of the monoclinic phase (PDF#70-1189). (C-D) SEM images of the as-synthesized sample.

We, however, observed the presence of broadened diffraction peaks. The broadening of the peaks was attributed to the formation of nano crystallite [36], which was confirmed by the SEM images in Figure 1 (C-D). Using the modified Scherrer method[37] (Eq.4) to calculate the average size of the crystallite through the representative peaks (with indexed diffractogram), the estimated average size of the crystallites obtained was 34 nm. The presence of nanocrystallites in the sample can cause the contraction of the lattice and the formation of more oxygen vacancies, thus favoring the occurrence of catalytic reaction[38-40]. This can be demonstrated in equation (4) below:

$$\ln \beta = \ln \frac{K\lambda}{D} + ln \frac{1}{\cos(\theta)} \qquad \text{Eq. 4}$$

where **β** is the peak width of the diffraction peak profile at half maximum height (radians), **K** is a constant related to the crystallite shape (0.9), **λ** is the X-ray wavelength (0.15406 nm), and **θ** is half the value of **2θ** peak position in the diffractogram.

The as-synthesized material exhibited a porous morphology, as shown in the SEM images (Figure 1 (C-D)). The pores were formed by irregularly shaped nanometric clusters, and channels could be found between the pores formed.

The dimensions of these structures were found to be between 14 to 75 nm in size, with average size of 43 nm (Figure S1). Based on the EDS analysis presented in the supplementary material (Figure S1), the V/Co ratio obtained was 1.07; this value is in perfect agreement with the theoretical stoichiometry of $Co_2V_2O_7$ and confirms the formation of single oxide phase observed in the XRD analysis (Figure 1B). Raman spectral analysis of the $Co_2V_2O_7$ samples (Figure S1) exhibited five spectral elements, which corresponded to the vibrational modes of vanadium-oxygen bonds[41]. The Tauc plot technique [42] was used to determine the band gap of the material from the diffuse reflectance spectrum. The value obtained from the extrapolation of the graph (Figure S1) was 2.7 eV. The material developed was found to absorb light at wavelength shorter than 460 nm (blue); this helped promote electrons from the valence band to the conduction band. An identical value was reported by Ghiyasiyan-Arani *et al.*[32] for nanostructured $Co_2V_2O_7$ photocatalysts. The results presented here show that a single oxide phase was obtained at milder conditions and without heat treatment.

After characterizing the synthesized material, the oxide was incorporated into the PL6 carbon matrix, as described in the experimental section. The incorporation of the oxide into the PL6 carbon (PL6C) matrix was analyzed using SEM images. Figure 2 presents the SEM images with 50,000x magnification for (A) PL6C, (B) 2.5% $Co_2V_2O_7$/PLC6, and (C) 15% $Co_2V_2O_7$/PLC6. Additional images of the composites investigated in this study can be found in the supplementary (Figure S2-S3).

It is worth noting that the PL6C matrix maintained its mesoporous morphology (Figure 2A) even after small amounts of oxide were added to its structure (Figure 2B). Unlike the 15% $Co_2V_2O_7$/PL6C sample (Figure 2C) which exhibited the formation of agglomerates in its structure (indicated by the arrows), the PL6C samples with lower oxide ratio (Figure 2B) did not exhibit such phenomenon. The analysis of the composites by EDS enabled us to confirm the successful incorporation of the material into the carbon matrix without any losses, where a composition similar to the nominal ratio was obtained (Figure S3).

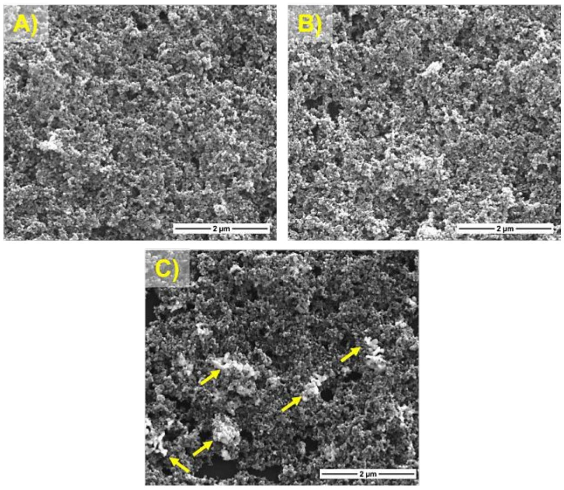

Figure 2. SEM images of (A) PL6C, (B)2.5% $Co_2V_2O_7$/PLC6, and (C) 15% $Co_2V_2O_7$/PLC6. The arrows at C) indicate the formation of agglomerates on the surface of the PL6C.

The valence states of Co, V, and O in $Co_2V_2O_7$ were analyzed by XPS measurement, presented in Figure 3. The Co 2p spectrum (Fig 3A) is composed by two species: Co^{2+} (780.0 eV) and Co^{3+} (781.9 eV) [43, 44]. The shake-up satellite presence (786.1 eV) also confirms the Co2+ species existence [35, 45]. The V 2p spectrum (Fig. 3B) presented the natural split of $2p^{3/2}$ and $2p^{1/2}$ peaks, but both indicates only V^{4+} species (516.7 eV in $2p^{3/2}$), since the peak positions of V^{5+} (523.7 eV) was not identified[45] . The O1s (Fig. 3C) showed two peaks which are correlated do metal-oxygen interaction (529.6 eV) and hydroxyl species or adsorbed water on the surface (532.2 eV)[46].

View Article Online
DOI: 10.1039/D2CP00072E

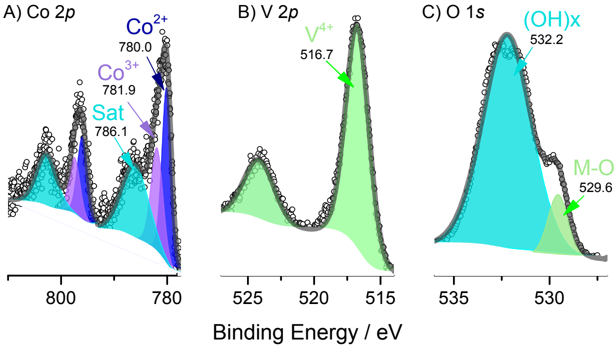

Figure 3. X-ray photoelectron spectra (XPS) of the C-$Co_2V_2O_7$: A) Co 2p, B) V 2p, and C) O 1s.

Electrochemical study of oxygen reduction reaction (ORR)

The electrochemical behavior of pure (bare) $Co_2V_2O_7$ in 0.1 M K_2SO_4 was evaluated. Figure S4a shows the voltammograms obtained from the microlayer of $Co_2V_2O_7$ deposited on glassy carbon and from the microlayer of the 2.5% $Co_2V_2O_7$/PL6C composite in a saturated solution of nitrogen or oxygen.

The voltammogram of the bare $Co_2V_2O_7$ (bare) immersed in nitrogen-saturated solution presented three reversible redox processes; this pattern of behavior has already been described in the literature [14, 35, 47]. The first and second processes that occur at +0.35 and +0.15 V are related to the process of reducing species from V(V) to V(IV), as already described in the literature[35, 47]. The second process at 0.0 V is related to the reduction of Co(II) to Co(I/0) [35, 47]. An analysis of the composite sample shows that the capacitive charge of carbon black suppresses the behavior of the oxide; as a result, one is unable to observe the presence of peaks related to $Co_2V_2O_7$. When the composite is inserted into a saturated O2 solution, a significant gain in current related to ORR is observed. This behavior was expected since this type of carbon exhibits a good ORR activity[11].

Given the above observations, a more detailed study was carried out in order to determine the number of electrons and the selectivity of the material for H_2O_2 using linear sweep voltammetry coupled to a rotating ring disk electrode (RRDE). The rotation speed (ω) of the system ranged between 100 and 2500 rpm. The results obtained from the application of 100, 400, 900, 1600 and 2500 rpm rotations for the $Co_2V_2O_7$/PL6C material in the ratio of 2.5, 5.0, 10, and 15% are presented in the supplementary material (Figure S4).

The rotation speed of 900 rpm was used to conduct a comparative analysis of the catalytic materials. The LSV plots (Figure 4) obtained had two parts: the upper part, which corresponded to the current values recorded on the ring, and the lower part, which corresponded to the current values recorded on the disk. The current values recorded on the disk were related to the ORR via two-electron ($2e^-$) or four-electron ($4e^-$) pathways, while the current values recorded on the ring were associated with the oxidation of H_2O_2. Three distinct regions can be observed in Figure 4. In the first region (potential range between +0.4 and -0.1 V), one observes the presence of only the capacitive current; this means that the ORR process is controlled by change transfer. In the second region (potential range between -0.1 and -0.55 V), the ORR is found operating in a mixed regime; in other words, the reaction is controlled by both change transfer and mass transport. In this region (second), the increase in the disk current causes a proportional increase in the ring current; to put it differently, the H_2O_2 electrogenerated in the disk is readily detected in the ring. In the third region (potential range between -0.55 and -0.8 V), the disk current can be found to record a maximum, constant value, and the reaction is controlled by mass transfer; in other words, the reaction is limited to the amount of O_2 that reaches the electrode.

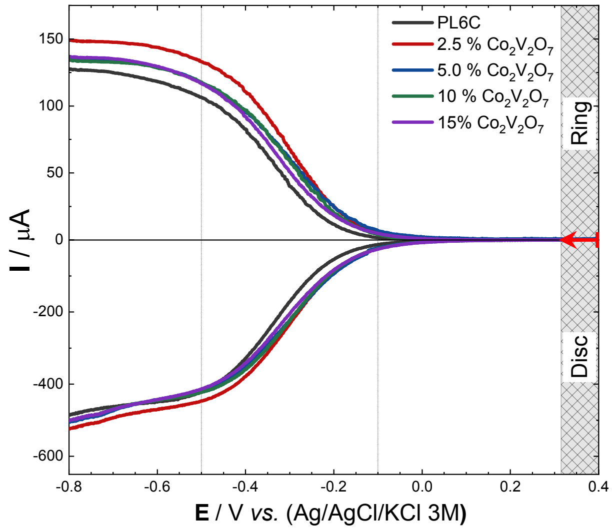

Figure 4. Linear sweep voltammograms for the $Co_2V_2O_7$/PL6C in the ratio of 2.5, 5.0, 10.0, 15.0% (w/w), and for the bare PL6C. The following conditions were employed: scan rate of 5 mV s^{-1}; ω = 900 rpm; 0.1 mol L^{-1} K_2SO_4 (with pH 2.5) saturated with O_2 was used as supporting electrolyte.

Looking at Figure 4, one will observe that all the modified $Co_2V_2O_7$/PL6C catalysts (with different percentages of $Co_2V_2O_7$) presented a profile very similar to the bare PL6C catalyst; however, there was a slight increase in the current values recorded in the ring, and this shows that there was a slight increase in H_2O_2 production in the modified microlayers. The bare PL6C presented a maximum current value of 127 µA. The 2.5% $Co_2V_2O_7$/PL6C catalyst exhibited the highest current value (150 µA), which was equivalent to a 16% increase in the amperometric current; this increase in current indicates an increase in H_2O_2 production for the composite. The 5%, 10% and 15% $Co_2V_2O_7$/PL6C catalysts recorded a smaller increase in current; the current values recorded were 5 to 7% higher than the current value of the bare PL6C. This smaller increase in current (for the 5%, 10% and 15% $Co_2V_2O_7$/PL6C catalysts) indicates that the agglomerates formed (Figure 4C) may have reduced the electroactive area of the microlayer, affecting the efficient production of H_2O_2. Similar results have already been obtained for other catalysts [5, 9]. In essence, the results show that the modification of PL6C with $Co_2V_2O_7$ improves the selectivity of the amorphous carbon matrix, most likely due to an increase in oxygen adsorption in the vacancies from the oxide defects, because no change in the reaction onset potential was observed, resulting in higher electrogeneration of hydrogen peroxide.

As pointed out by a number of studies reported in the literature, this improvement in hydrogen peroxide electrogeneration may be associated with the individual catalytic effects exhibited by cobalt oxide [15, 18] and vanadium oxide [16, 30]. According to reports in the literature, molecular oxygen interacts easily with cobalt in CoO_x/C [15]; this interaction also leads to a higher production of the intermediate •OOH, since cobalt has optimal bonding energy with •OOH[18]. The formation of this intermediate (•OOH) is the limiting step for H_2O_2 generation, once the other intermediaries (•OH and •O) do not lead to the production of H_2O_2. As for VO_x, the oxygen vacancies present on its surface tend to facilitate the adsorption of oxygen in this material by increasing the amount of oxygen adsorbed in it and promoting the activation of molecular oxygen[16, 30].

All the modified $Co_2V_2O_7$/PL6C catalysts presented almost similar ORR onset potential. These catalysts presented ORR onset potential close to -0.12 V *vs*. Ag/AgCl, which represents a positive shift of 50 mV from the potential of PL6C (-0.17 V *vs*. Ag/AgCl). This result implies that the modification of PL6C with $Co_2V_2O_7$ leads to a change in the onset potential of the reaction, with a reduction in the consumption of energy in the ORR process and improvement in selectivity. This shift in potential is associated with effects that have already been reported in the literature [15, 17, 18, 30].One of these effects is related to the intermediation of the transfer of electrons to the water molecule absorbed on the electrode surface by metal species that present smaller oxidation states caused by the reduction of the metals during polarization at the cathode.

Based on the current values recorded on the ring (i_a) and disk (i_d) of the RRDE, it was possible to calculate the efficiency of H_2O_2 generation ($X_{H_2O_2}$) and the number of electrons exchanged (n_t) in the ORR process, using Eqs. (5) and (6), respectively [4]:

$$X_{H_2O_2}(\%) = \frac{(200.i_a)/N}{(i_d + i_a)/N} \qquad (5)$$

$$n_t = \frac{4i_d}{(i_d + i_a)/N} \qquad (6)$$

where i_a is the current value recorded on the ring (in A); i_d is the current value recorded on the disk (in A); and N is the RRDE collection coefficient (value= 0.37; according to the information provided by the manufacturer). The two parameters, $X_{H_2O_2}$(%) and n_t, were calculated based on the average value obtained in the potential range of the mixed condition (-0.3 to -0.8 V). The graphs obtained for equations (5) and (6) related to the region of the mixed condition are shown in Figure S5. The average and maximum values obtained for $X_{H_2O_2}$(selectivity) and the average number of electrons involved in the reaction (n_t) for each condition studied are shown in Table 1; this table also presents the maximum current values recorded on the ring (i_{max}) and the percentage gain in current of the i_{max} compared to the current of the bare PL6C (%G_{PL6C}).

As can be seen in Table 1, the bare PL6C sample presented H_2O_2 (%) generation efficiency of 82%. This value means that 82% of the oxygen reduction reaction which occurred on the surface of the material generated H_2O_2 via $2e^-$, while the remaining 18% generated H_2O via $4e^-$. The value related to hydrogen peroxide generation efficiency obtained for the bare PL6C sample showed that the material was highly selective for the reaction of H_2O_2, and the modification of the material with $Co_2V_2O_7$ led to a further increase in ORR selectivity for H_2O_2. Among the modified samples investigated here, the 2.5% $Co_2V_2O_7$/PL6C catalyst promoted the highest selectivity with H_2O_2 electrogeneration of 92%, followed by 5, 15 and 10% $Co_2V_2O_7$/PL6C catalysts, which promoted H_2O_2 electrogeneration of 86%, 85%, and 82%, respectively.

View Article Online
DOI: 10.1039/D2CP00070F

Table 1: Values obtained in the interval of -0.3 to -0.8 V for the following: the maximum current recorded on the ring during H_2O_2 oxidation (i_{max}); the percentage gain in current of i_{max} compared to the current of PL6C (**%**G_{PL6C}); the average value ($\overline{X}_{(H_2O_2)}$) and maximum value ($X^{max}_{(H_2O_2)}$) of H_2O_2 generation efficiency; and the average value of the number of electrons involved in the reaction (n_t)

	i_{max} (μA)	**%**G_{PL6C}	$\overline{X}_{(H_2O_2)}$	$X^{max}_{(H_2O_2)}$	n_t
CPL6	127.6	-----------	82	84	2.4
2.5%	149.2	16.9	92	94	2.2
5.0%	135.0	5.8	86	89	2.3
10%	134.3	5.3	85	88	2.3
15%	131.9	3.3	80	88	2.3

In terms of the number of electrons transferred from the ORR, the bare PL6C sample recorded an average n_t value of 2.4 electrons, as seen in Table 1. Compared to the PL6C, all the materials modified with $Co_2V_2O_7$ presented a decrease in the value of n_t, with an average n_t value closer to 2 electrons. The 2.5% $Co_2V_2O_7$/PL6C catalyst exhibited the lowest n_t value (2.2 electrons), followed by the 5% $Co_2V_2O_7$/PL6C catalyst, 10% $Co_2V_2O_7$/PL6C catalyst, and 15% $Co_2V_2O_7$/PL6C catalyst with approximately 2.3 electrons. Thus, these results helped further confirm that the modification of PL6C with $Co_2V_2O_7$ oxide enhanced the selectivity of the amorphous carbon black matrix.

To gain a better understanding of the processes that occur during ORR and to evaluate the mechanism involving the reduction reaction, adsorption, activation and mass transport, electrochemical impedance spectroscopy measurements were performed at different potentials. To perform the spectral analysis, potentials were chosen from three different regions observed during the LSV analysis. These regions, which have already been described by our research group [11], are related to the adsorption/activation of oxygen on the surface of carbon and are limited by mass transport and the limiting current. For data adjustment purposes, an electrical equivalent circuit (EC) proposed by Kwon *et al.*[48] was employed; this electrical circuit is commonly used in the literature for this type of porous carbonaceous materials[11, 48-51]. The Nyquist spectra and Bode diagram obtained for the PL6C and 2.5% $Co_2V_2O_7$/PL6C catalysts at -0.2 V are shown in Figures 4A and 4B. The EC chosen to represent the physical model of the electrode is in the inset of Figure 5A. All the spectra obtained at different potentials and under different conditions are presented in the Supplementary Material (FigureS6).

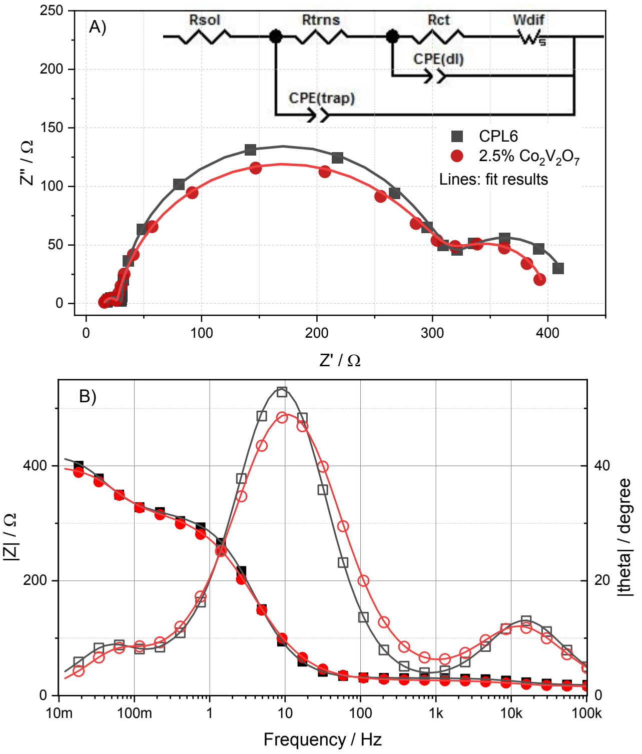

Figure 5. Nyquist and equivalent circuits (inset) used for adjusting the PLC6 and 2.5% $Co_2V_2O_7$ data (A). Bode Impedance Modulus and Bode Phase for PLC6 and 2.5% $Co_2V_2O_7$ (B). 0.1 mol L^{-1} K_2SO_4 (pH 2.5) saturated with O_2 was used as supporting electrolyte. The electrode was spun at 900 rpm.

The presence of a semi-circle in the high-frequency region (HF) of the Nyquist spectrum (see Figure 4A) is typical of the electronic properties of carbonaceous materials [41]. The predominant resistor-capacitor (**R-C**) circuit in this region was linked to the resistance to electron transfer ($\mathbf{R_{trns}}$) in the carbon matrix and the capacitance generated by electron trapping ($\mathbf{C_{trap}}$) in the surface defects. The presence of the R-C circuit, which was associated with the electrochemical properties of the material, and the Nernst diffusion impedance ($\mathbf{Z_{diff}}$), which was associated with the mass transport of the system[52], can be seen in the low frequency (**LF**) region. The charge transfer resistance ($\mathbf{R_{ct}}$) and double-layer capacitance ($\mathbf{C_{dl}}$) [48] were represented by the **R-C** circuit in the **LF** region. A Warburg impedance was used to describe the $\mathbf{Z_{diff}}$[52, 53]. The **EC** used in this study was based on the phase plot in Figure 4B's Bode diagram. For all potentials investigated, the **EC** elements were determined, and the $\mathbf{X^2}$ value obtained was always close to $1x10^{-3}$. Table S1 displays all of the data obtained from fitting the impedance spectra. Due to the system's non-ideality, both capacitances were regarded as constant phase elements (CPEs). The capacitance values from the CPE were obtained using the following formula (Eq. 7):

$$C = \frac{(R.Q)^{1/n}}{R} \qquad \text{Eq. (7)}$$

where ***Q*** is the CPE constant, ***n*** is the CPE exponent, and ***R*** is the corresponding **R-C** circuit resistance.

The $Co_2V_2O_7$-modified PL6C catalysts presented an improvement in their electronic properties. The values obtained from the fitting analysis showed that the modification of PL6C with $Co_2V_2O_7$ led to a decrease in $\mathbf{R_{trns}}$ and $\mathbf{C_{trap}}$. The calculated $\mathbf{R_{trns}}$ obtained for all the modified $Co_2V_2O_7$/PL6C materials (with 2.5%, 5%, 10%, and 15% of $Co_2V_2O_7$) were 9-13% lower than that obtained for the bare PL6C; this shows that there was an improvement in the composite conductivity following the incorporation of $Co_2V_2O_7$ into the carbon matrix. Shin *et al.* [50] reported similar effects when they modified graphene with MoFe nanoparticles. Based on the analysis of the relationship between $\mathbf{R_{trns}}$ and an increase in the amount of the modifier, it was noted that a 6-fold increase in the modifier led to an average decrease of 3.2% in $\mathbf{R_{trns}}$.

If the error in the simulations is considered, this decrease in conductivity can be said to have no significant effect. In essence, this implies that one can obtain the same effect in $\mathbf{R_{trns}}$ with the application of small quantities of the modifier. A similar variation was observed in $\mathbf{C_{trap}}$, which recorded a decrease of 4-17%. This change in $\mathbf{C_{trap}}$ shows that the modification of the matrix resulted in a reduction of the surface defects responsible for the trapping of the capacitance. The analysis of the values related to the R-C semi-circle in high frequency obtained for all the samples under different potentials showed that there was no significant variation among the samples. This behavior was expected, considering that the semi-circle corresponds to the electronic properties of the material, which should not vary significantly with the potential applied.

However, in the LF region (where the elements related to electrochemical performance were determined), the values obtained for the elements that indicate electrochemical efficiency were found to be dependent on the applied potential. Figure 6A shows the graph related to the relationship between the $\mathbf{R_{ct}}$ and $\mathbf{R_{diff}}$ calculated under the applied potential, and Figure 6B shows the relationship involving the $\mathbf{C_{dl}}$.

The electrochemical performance of the PL6C observed here is similar to that determined and described by our group in a previous paper[11]; basically, the behavior of the resistance is largely dependent on the applied potential. As can be noted in Fig. 5, the linear sweep voltammogram (line dark gray - top inset) exhibits three distinct regions. In the first region (I), between +0.1 and -0.1 V, one notices the presence of a capacitive current only. Due to the high $\mathbf{R_{ct}}$ value, the ORR is limited by the electron transfer process. The O_2 adsorption process occurs in this first region[11]. Looking at the second region, which lies between -0.1 and -0.5 V, one will observe that the ORR is governed by mixed kinetics - where the process is controlled by both charge transfer and mass transfer. Finally, in the last region (-0.5 to -0.8 V), one can see that the process is controlled by oxygen diffusion from the bulk solution to the electrode interface.

Another observation worth mentioning is that, in the activation region, where adsorption occurs, the $Co_2V_2O_7$–modified PL6C catalysts presented relatively higher values of resistance and C_{dl} compared to the bare PL6C. It is worth noting that the double-layer capacitance provides us with a clearer idea regarding the changes in the electrode surface, and this is directly correlated with O_2 adsorption under the applied potential. Compared to the bare PL6C, the slightly higher C_{dl} obtained for $Co_2V_2O_7$/PL6C shows that there must be free sites for O_2 adsorption in the modified material; this implies that the modification of the carbon matrix with $Co_2V_2O_7$

causes a decrease in the amount of O_2 adsorbed under the potentials applied[11]. This decrease in the amount of O_2 adsorbed explains why the PL6C exhibits a higher disk current during scanning than the modified PL6C (Figure3).

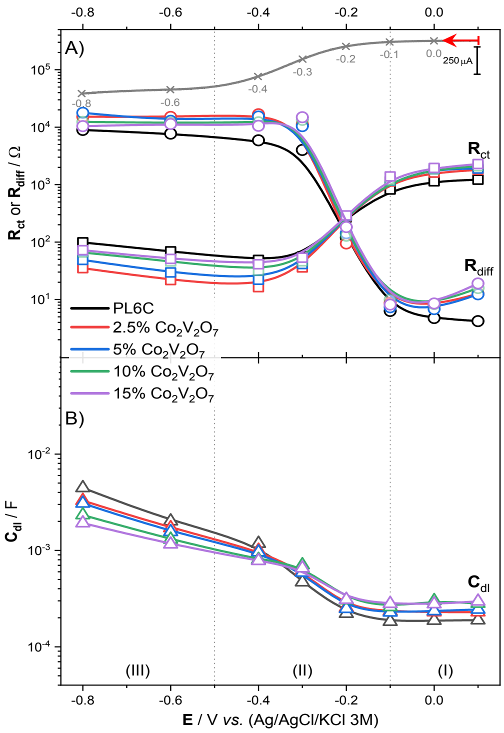

Figure 6. Impedance parameters: charge transfer resistance [square in (A)], diffusional resistance [circle in(A)], and double layer capacitance [triangle in (B)] in relation to the applied potential and LSV curve at 900 rpm (inset at the top) [gray line in (A)].

In the second region (II), we observed that when the O_2 reduction potential was reached, there was an improvement in the electrochemical performance of the $Co_2V_2O_7$/PL6C catalysts. The decrease in $\mathbf{R_{ct}}$ values recorded for the PL6C-modified materials was more significant than that observed for the bare PL6C. At -0.4 V, the $\mathbf{R_{ct}}$ values obtained for 2.5% $Co_2V_2O_7$/PL6C and PL6C were 16.4 and 68.6 Ω, respectively (Table S1). As expected, the $\mathbf{R_{diff}}$ value increases under more negative potentials; this is due to the consumption of O_2 on the electrode surface. The consumption of O_2 on the electrode surface causes the diffusion of O_2 dissolved in the solution to be adsorbed in the matrix; in other words, higher $\mathbf{R_{diff}}$ values translate into more oxygen consumption. In this scenario, the modification of PL6C with $Co_2V_2O_7$ yields comparatively better results compared to the application of bare PL6C.

Furthermore, in the second region, it is also possible to calculate the number of electrons for ORR by the method proposed by Tan *et al.* [54]. The number of electrons can be calculated by the ratio between the slopes from the variation of $\mathbf{R_{diff}}$ and $\mathbf{R_{ct}}$. The data used for performing this calculation and the values obtained by linear regression are shown in Table S2. Using the method described earlier, the number of electrons obtained for 2.5% $Co_2V_2O_7$/PL6C and PL6C was 2.1 and 2.4, respectively; these values are in perfect agreement with those calculated in Equation 6 based on the experiments conducted using RRDE.

View Article Online
DOI: 10.1039/D2CP00072F

As expected, the process in the last region (-0.55 to -0.8 V - III) is controlled by the diffusion of oxygen, with $\mathbf{R_{diff}}$>>$\mathbf{R_{ct}}$. Thus, the $\mathbf{R_{diff}}$ value obtained for 2.5% $Co_2V_2O_7$/PL6C was higher than that of PL6C. The current recorded for 2.5% $Co_2V_2O_7$/PL6C was lower than that of PL6C in this region due to the lower diffusion of oxygen.

Electrogeneration of hydrogen peroxide

Based on the electrochemical analysis of ORR, with the application of the hydrodynamic system using RRDE and EIS, the 2.5% $Co_2V_2O_7$/PL6C was found to enhance the electrogeneration of H_2O_2. In view of that, a GDE modified (GDEm) with 2.5% $Co_2V_2O_7$/PL6C and an unmodified GDE (containing PL6C only) were prepared aiming at investigating the *in situ* generation of H_2O_2 in gas diffusion electrode. The GDE allows the cathodic reduction of $O_{2(g)}$ via 2e$^-$ at the triple interface gas/electrode/solution, promoting the production of H_2O_2. In addition, the use of GDE leads to greater efficiency compared to conventional electrodes (flat electrodes) since this electrode does not suffer from the limitations caused by the low solubility of O_2. GDE is known to be highly porous; this electrode has a structure composed of a wide variety of channels within its 3D structure which allows the flow of O_2 gas between the channels. These channels allow O_2 to be diffused in the electrode and interact with the catalytic particles present in the conducting matrix; this mechanism allows the catalytic particles to take part in the ORR.

The analysis of H_2O_2 electrogeneration using GDEs was carried out by electrolysis under constant current densities of 25, 50, 75 and 100 mA cm^{-2}. The results obtained related to H_2O_2 electrogeneration for the unmodified GDE and modified GDE (GDEm) are shown in Figure 7.

Both the modified and unmodified GDEs presented profiles with linear growth of electrogenerated H_2O_2 in the first 30 minutes of electrolysis (Figure 7A-B). After 60 minutes of electrolysis, the electrogeneration of H_2O_2 became practically constant. This effect can be attributed to the balance between the reactions that occur at both the cathode and the anode. The main reaction that occurs in the system is the formation of H_2O_2 in the working electrode (cathode) from the ORR via 2e$^-$ pathway. One will note, however, that this generated H_2O_2 can be reduced again via 2 extra electrons, with the generation of H_2O (Eq. 8), or the H_2O_2 species can be oxidized at the anode, generating O_2 molecules (Eq. 9). The first equation depends on the hydrogen peroxide concentration produced at the cathode only; in other words, the greater the amount of hydrogen peroxide produced, the more significant the contribution of this parasitic process. The second equation also depends on the diffusion of H_2O_2 to the bulk solution.

$$H_2O_2 + 2H^+ + 2e^- \rightarrow 2H_2O \qquad (8)$$

$$H_2O_2 \rightarrow O_2 + 2H^+ + 2e^- \qquad (9)$$

Apart from these electrochemical reactions, chemical decomposition reactions of H_2O_2 can be observed within the solution. At high concentrations of H_2O_2, these species can react with each other to form O_2 and H_2O molecules (Eq. 10).

$$2H_2O_2 \rightarrow O_2 + 2H_2O \qquad (10)$$

View Article Online
DOI: 10.1039/D2CP00072E

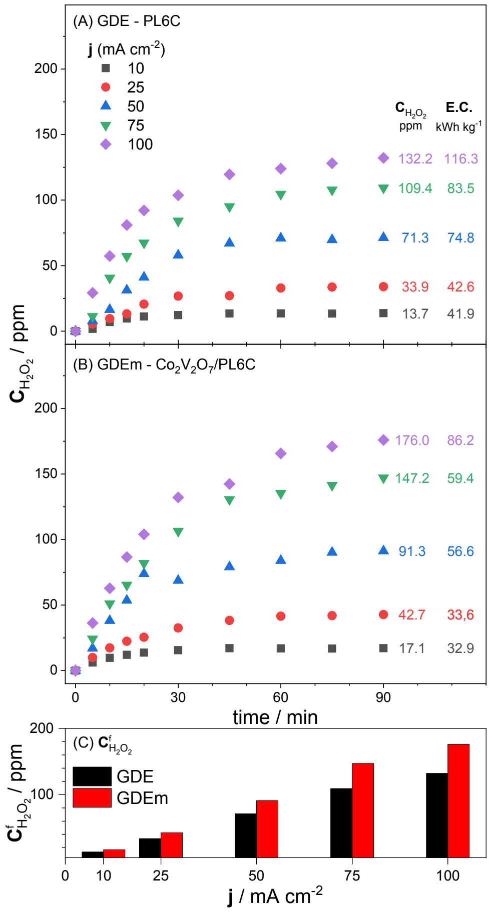

Figure 7. Hydrogen peroxide electrogenerated as a function of time for PL6C – GDE (A) and 2.5 % $Co_2V_2O_7$/PL6C – GDEm (B) during a 90-minute electrolysis. Supporting electrolyte: 0.1 mol L^{-1} K_2SO_4 (pH 2.5) with O_2 flow at 0.2 bar.

Thus, increasing the current does not always generate a proportional increase in H_2O_2 production [5]. This occurs because the combination of H_2O_2 electrogeneration with the three parasitic reactions will determine the maximum concentration of H_2O_2 produced in the bulk solution.

The analysis of the final concentration of H_2O_2 ($C^f_{H_2O_2}$) *vs.* current density (see Figure 7C) shows that there was an increase in $C^f_{H_2O_2}$ when the current was increased. However, higher currents (75 and 100 mA cm^{-2}) corresponded to a relatively lower increases in the $C^f_{H_2O_2}$compared to the higher increases in $C^f_{H_2O_2}$ observed for the smaller currents (10 to 50 mA cm^{-2}). This behavior can be associated with the parasitic reactions explained above.

At low current densities (10 and 25 mA cm^{-2}), the amount of H_2O_2 electrogenerated was small; this is attributed to the fact that the charge applied to the GDEs interphase was not enough to reduce all the oxygen present. This shows that under these conditions of low current densities, the system is controlled by electron transfer. An increase in the applied current density leads to an increase in the amount of H_2O_2 electrogenerated in the system; in other words, there is a mixed control of electrogeneration through electron transfer and parasitic reactions. However, when a high current density (100 mA cm^{-2}) is applied, although the final concentration of H_2O_2 keeps increasing, the growth rate decreases; this shows that parasitic reactions play a more significant role in the system. The maximum concentration of H_2O_2 obtained for the unmodified GDE was 132 mg L^{-1} in 90 min of reaction at a current density of 100 mA cm^{-2}. For the GDEm (modified with 2.5 % $Co_2V_2O_7$/PL6C), an increase of 35% in H_2O_2 electrogeneration was observed (176 mg L^{-1}) at the same current density (100 mA cm^{-2}). In general, the production of H_2O_2 in GDEm was 25 to 35% higher than in GDE.

Other essential factors that must be taken into account when analyzing gas diffusion electrodes are the apparent rate constant of H_2O_2 formation (**k_{ap}**) and the energy consumption (**E.C.**). The **k_{ap}** can be calculated by assuming that the formation reaction (Eq. 1) has zero pseudo-order kinetics. Thus, the **k_{ap}** is calculated from the linear region (see Figure 7), where the contributions of parasitic reactions are low. The angular coefficients for these regions represent **k_{ap}** according to equation (11), where $C_t^{H_2O_2}$ is the concentration of H_2O_2 at time (t). To obtain the **E.C.** values related to H_2O_2 electrogeneration, the following formula (Eq. 12) was used:

$$C_t^{H_2O_2} = k_{ap}.t \qquad \text{(Eq. 11)}$$

$$E.C. = \frac{i.E.t}{m} \qquad \text{(Eq. 12)}$$

where ***E.C.*** is the energy consumption in *kWh kg*$^{-1}$, ***i*** is the current in *A*, **E** is the cell potential in *V*, **t** is the time in hours, and **m** is the mass of H_2O_2 electrogenerated in *kg*. In Figure 8, one can see the relationship between **E.C.** and current density, along with the percentage ratios related to **k_{ap}** and H_2O_2 concentration in 20 and 90 min of treatment obtained for the GDEm and GDE.

Both samples presented a similar pattern of behavior in terms of energy consumption - as the applied current density increased, energy consumption also increased. This behavior can be attributed to the fact that the increased charge applied at the GDE interface favors the parasitic reactions (Eq. 8-10).

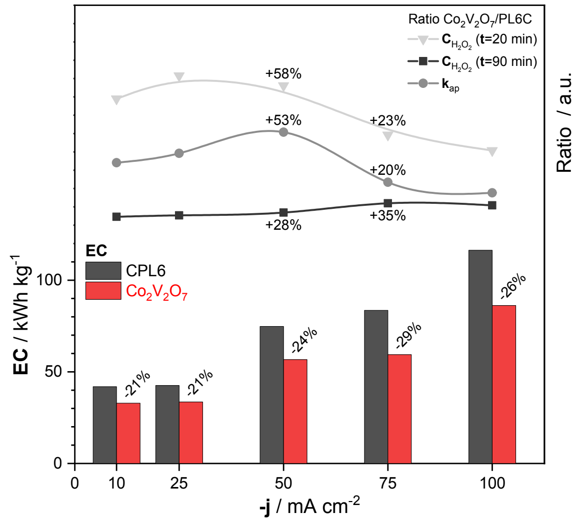

Figure 8. Graph of energy consumption as a function of current density for GDE and GDEm (2.5% $Co_2V_2O_7$/PL6C). Top inset: comparative analysis of GDEm and GDE based on the ratio of k_{ap} (●) and H_2O_2 concentration in 20 (▼) and 90 min of treatment (■). Supporting electrolyte: 0.1 mol $L^{-1}$$K_2SO_4$ at pH 2.5, with O_2 flow at 0.2 bar.

An analysis of the **E.C.** values for the GDEm as a function of current density shows that the application of the current density of 100 mA cm^{-2} led to an increase of approximately 10% in energy

View Article Online
DOI: 10.1039/D2CP00078F

consumption (26.8 kWh kg^{-1}) and a small increase in electrogenerated H_2O_2 (28.8 mg L^{-1}) compared to the current density of 75 mA cm^{-2}. This may imply that there was an increase in parasitic reactions when the current density of 100 mA cm^{-2} was applied. Based on this result, the best charge distribution chosen for the GDE interface was the current density of 75 mA cm^{-2}; this density was chosen due to its efficiency both in terms of H_2O_2 electrogeneration and energy consumption. It is worth mentioning that, under all the current densities investigated, the GDEm presented values of energy consumption which were between 21 and 29% less than those of the GDE; this confirms that the modification of Printex L6 carbon with $Co_2V_2O_7$ oxide resulted in significant improvements in the energy efficiency of the material.

The reaction reached a steady state after 90 minutes of electrogeneration. When the calculated $\boldsymbol{C}^{t}_{H_2O_2}$ratios for densities of 50 and 75 mA cm^{-2} are compared, the values obtained for (t = 20 and 90 min) show different patterns of behavior. The concentration of the finished product increases by about 10%. However, in the linear region (up to 20 min), where the contributions of parallel reactions were low, the accumulation of H_2O_2 in the solution decreased by about 50% with increasing current density during the first 20 minutes. At a current density of 50 mA cm^{-2} and after 20 minutes of reaction, the difference in H_2O_2 concentrations between the GDEm and GDE was 1.58; at a current density of 75 mA cm^{-2}, the difference was reduced to 1.23. This behavior was found to be distinct from that observed for the ratio at the conclusion of the experiment. This outcome can be attributed to the fact that H_2O_2 is consumed in order to produce •OH.

Zhang *et al.*[29] had already identified the activation of H_2O_2 on the $Co_2V_2O_7$ surface; in their study, the authors highlighted the ability of $Co_2V_2O_7$ nanoparticles to act as heterogeneous catalysts for the formation of •OH radicals via H_2O_2 added to the reaction medium. The ESR experiments demonstrated the ability of $Co_2V_2O_7$ nanoparticles to convert H_2O_2 to •OH. Leonard et al.[47] have also shown that cobalt can be used to mediate the generation of reactive oxygen species.

At the beginning of the reaction, the higher H_2O_2 production in the GDEm causes an increase in H_2O_2 concentration within the electrode channels. The higher the concentration of H_2O_2 in the electrode's channels, the more likely it is that the H_2O_2 produced will come into contact with the oxide, activating it and generating •OH radicals. However, the majority of the H_2O_2 produced is released into the bulk solution, where it will be concentrated until the equilibrium between the formation and parallel reactions is reached. Another important factor to note is that there was no significant increase in k_{ap}, which was expected for GDEm. At a current density of 75 mA cm^{-2}, the k_{ap} increased by only 23% when a more than two-fold increase was expected [5, 55].

When one compares the calculated ratios for the densities of 50 and 75 mA cm^{-2}, the values obtained for $\boldsymbol{C}^{t}_{H_2O_2}$(t = 20 and 90 min) presented different patterns of behavior. After 90 min of experiment, the reaction reached a stationary equilibrium, and the final concentration ($\boldsymbol{C}^{90\,min}_{H_2O_2}$) presented an increase of about 10%. However, in the linear region (up to 20 min), where the contributions of parallel reactions were low, one will observe a decrease of about 50% in the accumulation of H_2O_2 in the solution with the increase in current density during the first 20 min. At the current density of 50 mA cm^{-2} and in 20 min of reaction, the difference in terms of H_2O_2 concentrations between the GDEm and GDE was 1.58; this difference reduced to 1.23 at the current density of 75 mA cm^{-2}. This behavior was found to be different from that observed for the ratio at the end of the experiment. This outcome can be attributed to the fact that H_2O_2 is consumed in order to produce •OH. The activation of H_2O_2 on the $Co_2V_2O_7$ surface has already been observed and described by Zhang *et al.*[29]; in their study, the authors pointed out the ability of $Co_2V_2O_7$ nanoparticles to act as heterogeneous catalysts for the formation of •OH radicals through H_2O_2 which had been added to the reaction medium. The results obtained from the ESR experiments performed by demonstrated the ability of $Co_2V_2O_7$ nanoparticles to convert H_2O_2 to •OH. Leonard *et al.*[18] have also demonstrated the use of cobalt to mediate the generation of reactive oxygen species.

At the beginning of the reaction, the higher production of H_2O_2 in the GDEm leads to an increase in the concentration of H_2O_2 within the electrode channels. The higher the concentration of H_2O_2 in the channels of the electrode, the higher the probability that the H_2O_2 produced comes into contact with the oxide, which is capable of activating it and generating •OH radicals. However, most part of the H_2O_2 produced is released into the bulk solution where H_2O_2 will be concentrated until it reaches the equilibrium between the formation reactions and the parallel reactions. Another relevant factor that is worth mentioning is that there was no significant increase in $\mathbf{k}_{ap}$ as it was expected for GDEm. At the current density of 75 mA cm^{-2}, the $\mathbf{k}_{ap}$ recorded an increase of only 23% when more than 2-fold increase was expected [5, 55].

Analysis of repeatability and metal dissolution

After the analysis of H_2O_2 electrogeneration, the repeatability of GDEm was analyzed based on the application of six cycles of H_2O_2 electrogeneration in different days; the loss of $Co_2V_2O_7$ through acid leaching was investigated at the end of each cycle.

Figure S7 shows that there was a slight loss in H_2O_2 production between the first and second use of the modified electrode; nonetheless, the amount of H_2O_2 generated after the second use practically remained constant. Based on the results obtained from the application of graphite-furnace atomic absorption spectrometry (GF/AAS) under the standard addition method, the cobalt and vanadium concentrations obtained were less than 0.75 μmol L^{-1} at the last cycle of H_2O_2 production. The total mass loss during the six cycles of H_2O_2 electrogeneration was less than 0.05% of the initial mass of $Co_2V_2O_7$. These results show that the material was stable under the conditions studied, and there were no significant losses in performance and composition after four cycles of H_2O_2 electrogeneration.

Using GDEm for the efficient removal of methyl-paraben

The analysis of the efficiency of MeP removal was conducted using a solution containing the supporting electrolyte and initial concentration of 30 mg L^{-1} MeP. This analysis was performed aiming at finding out the following: i) whether $Co_2V_2O_7$ can exhibit a mimetic behavior of peroxidase nanoenzyme, as reported by Zhang *et al.*[31], promoting the generation of •OH radical as a Fenton-like catalyst in GDEm; and ii) whether the photo-generated electron in

View Article Online
DOI: 10.1039/D2CP00072E

$Co_2V_2O_7$ can collaborate with the generation of •OH radical, as reported by Zhao *et al.*[12] for MOFs with Co oxides. The removal of MeP was investigated based on the application of the following treatment processes: photo-degradation (UV) only, electrogeneration of H_2O_2 (e-H_2O_2), and electrogeneration of H_2O_2 activated by UV light (e-H_2O_2+UV). The experiments were carried out using both electrodes (GDE and GDEm); the results obtained (in terms of MeP degradation) are shown in Figure 9A. The graphical representation of the kinetic rates and the UV spectra can be found in Figure S8.

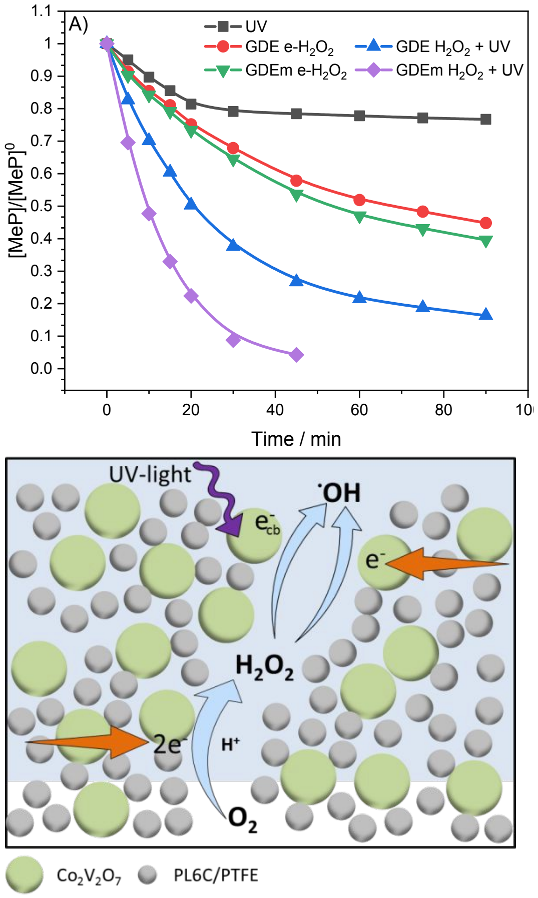

Figure 9. Degradation of methyl-paraben using different removal techniques and conditions: photo-degradation (UV) process and electrochemical process using GDE or GDEm in the presence/absence of UV light. The electrochemical processes were carried out at the current density of 75 mA cm^{-2}, using O_2-saturated 0.1 mol L^{-1} K_2SO_4 at pH 2.5 as supporting electrolyte. The O_2 pressure applied in the GDE was 0.2 bar, and a 5 W monochromatic UV lamp was used to perform the experiments. (A) A schematic illustration of the electrogeneration and activation of H_2O_2 based on the application of e-H_2O_2+UV|GDEm in acidic condition (B).

Under the photodegradation condition, only 23% MeP was removed; a study reported in the literature based on the application of this degradation process also recorded a similar value[56]. With regard to the application of the e-H_2O_2 process using GDE and GDEm, the use of GDEm promoted MeP removal of almost 10% higher than the GDE (62% for the GDEm and 53% for the GDE) and both electrodes recorded similar kinetic rates (2.1x10^{-4} and 2.3x10^{-4} s^{-1} for GDE and GDEm, respectively). Under the e-H_2O_2 process, the compound removal was promoted by the hydroxyl radicals generated from the homolysis of electrogenerated H_2O_2; considering that the difference in terms of H_2O_2 production was small (less than 2x), the values related to MeP removal and the kinetics of homolysis were expected to be similar [6]. In other words, as the increase in H_2O_2 production was only 1.35x, the reaction depended more on the kinetics of homolysis than on the amount of H_2O_2 produced, since the production of H_2O_2 in both electrodes (GDE and GDEm) was similar. To investigate the influential role played by H_2O_2 in the compound removal, the degradations were tested in the presence of hydrogen peroxide only. The degradation of MeP was carried out in a reactor without GDEs, and H_2O_2 was added in the medium with concentrations close to those obtained in the presence of GDEs (100 and 150 ppm). Figure S10a shows the UV/Vis spectra obtained after 90 min of treatment in the presence and absence of GDEs. In the condition without GDE, where only H_2O_2 was added, the difference between the removal rates was only 3%. The MeP removal rates obtained in the presence of the GDE and GDEm were 53% and 62%, respectively. Looking at Figure S9a, the variation in terms of removal rates between the GDE and GDEm was expected to be close to 3%, but the difference observed was 3x higher. Part of this additional difference may be associated with the small portion of H_2O_2 which was activated in $Co_2V_2O_7$ in the electrode channels during the diffusion to the solution. As observed by Zhang *et al.*[31], $Co_2V_2O_7$ was able to activate a small part of the hydrogen peroxide produced.

In contrast, under the e-H_2O_2+UV process, the GDE and GDEm presented significant differences in terms of kinetic rates and MeP removal. The kinetic constant obtained for the GDEm was about 10x higer than that of the GDE (5.4x10^{-4} and 4.3x10^{-3}s^{-1} respectively). Furthermore, the use of the GDE resulted in MeP removal rate of approximately 80% after 90 min of treatment. The GDEm, on the other hand, recorded MeP removal rate superior to 95% after only 45 min of treatment. A comparison of the removal rates in 45 min of treatment showed that the difference observed in terms of MeP removal rate between [H_2O_2+UV|GDEm] and [H_2O_2+UV|GDE] was superior to 30%. To better understand this difference of 30%, experiments were conducted in the absence of GDEs (just as performed in the e-H_2O_2 process) but with the addition of H_2O_2 (100 and 150 ppm) in the medium and in the presence of UV light; the spectra obtained after 90 min of treatment are shown in Figure S9b. Looking at Figure S10b, one will observe that the variation in MeP removal, in the condition in which H_2O_2 was added and in the absence of GDEs, was 6% after the first 45 min of treatment; interestingly, this variation in MeP removal for the [H_2O_2+UV|GDEm] and [H_2O_2+UV|GDE] processes was 30%. The increase in MeP removal observed in the e-H_2O_2+UV process was higher than that observed in the e-H_2O_2 process. This difference can be associated with the synergism between the major activation of H_2O_2 from UV light and the minor activation derived from the effects that have already been described by other authors – these effects include the following: *i*) the capacity of mediation of $Co_2V_2O_7$ in the activation of hydrogen peroxide [31]; and *ii*) the capacity of the photo-generated electrons to also activate H_2O_2 [12] since the band gap of the synthesized material was 2.67 eV (see Figure S3).

The MeP mineralization rate obtained based on the values of the total organic carbon collaborates with the following hypotheses: H_2O_2 is activated by Co2V2O7 along the GDEm channel and on the surface of the GDEm, once the MeP removal rate obtained under the [H_2O_2+UV] process was 8 and 5% for GDEm and GDE, respectively, after 45 min of treatment. After 3 hours of treatment, the mineralization rate rose to 87% for GDEm and only 41% for GDE. This difference in mineralization rate indicated that the H_2O_2 generated in the GDEm was activated more than in the GDE under the same current and lighting conditions.

It is noteworthy that processes based on e-H_2O_2+UV do not quickly remove organic pollutants [1, 5, 6]. Generally, high rates of compound removal have only been obtained under electro-Fenton processes, where Fe(II) is introduced in solution for the activation of H_2O_2; this means that the GDEm developed in this study enhanced the electrogeneration of H_2O_2 and activated a portion of this electrogenerated H_2O_2. One needs to point out that while it is true that this observed effect – where bimetallic oxides act as Fenton-like catalysts, has already been reported in MOFs [12], this is the first time the effect is reported under the application of GDEs. Another interesting finding that is worth mentioning is that there was a relatively lower leaching of cobalt and vanadium in the GDEm – the total leaching observed after 12 hours of use was less than 0.05 %; this result rules out any possible occurrence of heterogeneous or homogeneous catalysis in the solution. Figure 9B presents a schematic illustration of the formation and activation of H_2O_2 in the GDEm under the H_2O_2+UV|GDEm process.

Experimental

Materials: All the chemical reagents used for the synthesis of cobalt vanadate, including ammonium metavanadate, cobalt(II) nitrate hexahydrate, ammonium hydroxide, and nitric acid, were of analytical grade and were used as received without further purification. Deionized water was used throughout the experiments.

Synthesis of cobalt vanadate: $Co_2V_2O_7$ was obtained based on the application of a technique adapted from the method proposed by Baudrin *et al.*[57]. Co-precipitation was carried out by the neutralization of solutions containing the precursors. To perform this synthesis, two 20 mL solutions were prepared using the following compositions: A) 1.0 M HNO_3 + 0.2 M $Co(NO_3)_2$; and B) 1.0 M NH_4OH + 0.2 M NH_4VO_3. The solutions were transferred into different containers and heated to a temperature of 80ºC. Upon reaching the temperature of 80ºC, the transfer was carried out dropwise, adding solution A to solution B. During the blending of the solutions, the system was kept under agitation. After the complete transfer of the solutions, the material was filtered, washed several times with deionized water, and dried at 120ºC. The steps involved and the scheme illustrating the synthesis of the material (cobalt vanadate) are shown in Figure 1A.

Characterization: The crystalline phase of the materials was characterized by X-ray diffraction (XRD) using a Shimadzu diffractometer model XRD-6000 (Cu Kα standard radiation: 1.5406 Å). The morphology and elemental composition of the composite were analyzed by high-resolution field emission scanning electron microscopy with energy dispersive spectrometry (FE-SEM, Zeiss Supra 35). Raman spectra analysis was carried out using Horiba iHR 550 spectrophotometer at 544 nm.

Electrode preparation and electrochemical measurements: The $Co_2V_2O_7$ oxide was added to Printex L6 carbon (PL6C) by physical adsorption in the proportions of 2.5, 5.0, 10.0, and 15.0 % (w/w). To perform this procedure, both catalytic masses were mixed with isopropyl alcohol under magnetic stirring for 40 min; the mixture was then dried in an oven for 3 h, where the temperature of 60 ºC was applied for the first two hours and the temperature of 100 ºC was applied in the last one hour.

The electrochemical measurements were performed based on the porous microlayer technique using the glassy carbon disk electrode (RRDE working electrode). The microlayer was prepared using a 25 µL drop of the $Co_2V_2O_7$/PL6C dispersion, which was previously prepared by mixing 1.0 mg of the catalytic mass with 1 mL of an aqueous Nafion® (0.05%) solution.

The ORR analyses were conducted using linear sweep voltammetry (LSV) in the potential range of +0.4 to -0.8 V *vs.* Ag/AgCl/KCl 3M, with scanning speed of 5 mV s^{-1}. A fixed potential of +1.0 V was applied on the RRDE platinum ring. For each LSV measurement, the electrode was rotated at constant speeds of 100, 400, 900, 1600, and 2500 rpm.

To perform the EIS analysis, the electrode was rotated at 900 rpm and the experiments were performed in the presence of saturated $O_{2(g)}$, using DC potentials of -0.8, -0.6, -0.4, -0.3, -0.2, -0.1, 0.0, +0.1 V, with AC modulation of 10 mV and frequency range of 100 kHz to 10 mHz. The data were recorded at 10 points per decade. All the EIS spectra were curve-fitted using the ZView software. EIS and ORR analyses were performed using a potentiostat/galvanostat (Metrohm Autolab PGSTAT-128N) equipped with FRA32M and RRDE Pine Instruments modules. The ring disk electrode was composed of a glassy carbon disk (0.2476 cm^2) and a platinum ring (0.1866 cm^2) with a collection factor of 0.37. The experiments were conducted using a three-compartment cell which consisted of the following: one compartment for the reference electrode connected with a Lugin capillary to the central compartment which contained the RRDE, and a compartment separated, by a junction, for the auxiliary electrode. An amount of 150 mL of 0.1 mol L^{-1} K_2SO_4 (pH 2.5, adjusted with H_2SO_4) saturated with O_2 or N_2 was used as supporting electrolyte.

Electrogeneration of H_2O_2 using GDEm: Based on the electrochemical studies, the quantitative analysis of H_2O_2 electrogeneration was performed using the GDE modified with 2.5 % $Co_2V_2O_7$/PL6C (GDEm). The unmodified GDE - which contained only PLC6, and the GDEm (7 cm^{-2}) – which contained $Co_2V_2O_7$/PL6C, were prepared based on the hot pressing technique using a steel mold, according to the procedures described in previous works[5, 9, 16]. Electrochemical assays of the GDEm were performed using a single compartment electrochemical cell composed of a working electrode (GDEm or GDE), a platinum counter electrode, and a Ag/AgCl/3M KCl reference electrode. An amount of 250 mL of 0.1 mol L^{-1} K_2SO_4 (pH 2.5, adjusted with H_2SO_4**)** was used as supporting electrolyte (with the GDE) under 0.2 bar of O_2 flow. Electrolysis was carried out at current densities of 25, 50, 75, and 100 $mAcm^{-2}$ for 90 min. The quantification of the electrogenerated H_2O_2 was performed by UV-Vis absorption spectrophotometry[5, 9, 16]. The analysis of dissolved metals concentrations was performed by atomic absorption spectrophotometry (AAS, Perkin Elmer PinAAcle 900T).

Methyl-Paraben (MeP) removal: Considering that metals immobilized in MOFs have been found to present Fenton-like catalytic effect [12, 22] and $Co_2V_2O_7$ has been demonstrated to have the ability to generate •OH radicals through the activation of H_2O_2, the MeP degradation experiments were performed in order to find out whether $Co_2V_2O_7$ immobilized in GDEm is capable of operating as a Fenton-like catalyst [31]. For the MeP removal analysis, the following condition was applied: initial concentration of MeP of 30 mg L^{-1} in 250 mL of 0.1 M K_2SO_4(pH 2.5). The following treatment processes were employed for the removal of MeP: photo-degradation (UV) and electrochemical degradation using GDE or GDEm in the presence/absence of UV light. The electrochemical processes were carried out at the current density of 75 mA cm^{-2}. The GDE was pressurized using O_2 at 0.2 bar, and a UV Pen-Ray mercury lamp 90-0012-01 (25 mA AC) was used as the light source. The UV Pen-Ray mercury lamp has typical intensity of 254 and 365 nm at 4.7 and 0.2 mW cm^{-2}, respectively. The lamp was inserted into a quartz tube at 1 cm distance from the surface of the GDEs. The cell was covered with a reflective material to avoid irradiation losses, and the solution temperature was kept at 25 °C. Finally, the solution was analyzed using a UV–Vis spectrophotometer (Shimadzu, UV-1900) with absorption peak intensity of 255 nm. The amount of MeP removed (%) was calculated using the following equation:

$$MeP\ Removal\ (\%) = {C_t}/{C_0} \times 100\% \quad \text{Eq. 3}$$

where C and C_0 refer to the concentrations of MeP solution at a specific time and at time 0, respectively.

Conclusions

The one-step green synthesis route applied in this study enabled us to obtain cobalt vanadate ($Co_2V_2O_7$) in the monoclinic phase, formed by nanocrystalline particles, without secondary phases. The environmentally friendly technique applied, which does not involve the use of organic solvents or heat treatment, was able to produce a highly efficient catalytic material with good electrochemical properties.

The incorporation of $Co_2V_2O_7$ into the PL6C matrix led to a marked increase in H_2O_2 production. The results obtained from EIS analyses showed that the modifier increases the electrochemical performance of the composite by improving the electronic and electrochemical properties of PL6C. In this way, the application of the proposed material yielded an increase of 94% in selectivity for hydrogen peroxide formation. The number of electrons involved in the reaction under the application of the modified composite in optimal conditions was 2.2, while the number of electrons involved in the reaction under the application of PL6C was 2.4. The proportion of the modified $Co_2V_2O_7$/PL6C that presented the best performance was 2.5% w/w.

The GDEm constructed under the optimal conditions described in the study increased H_2O_2 electrogeneration by 34% (with an energy consumption of 50 kWh kg^{-1}) compared to the conventional GDE. During the degradation of MeP, $Co_2V_2O_7$ was found to act as a Fenton-like catalyst in the GDEm; this pointed to the high application potential of GDEm for the successful degradation of compounds without the need of adding Fe(II) in the treatment process. The findings of this study showed that the application of the proposed $Co_2V_2O_7$-modified PL6C can improve the efficiency of GDEm.

Author Contributions

Study design: M.F.G., P.J.M.C, M.R.V.L;
Experimental work: M.F.G., P.J.M.C, P.G.C;
Data analysis and interpretation: All authors;
Manuscript preparation: All authors;
Manuscript editing: M.F.G., P.J.M.C;
Manuscript review: All authors.

Conflicts of interest

There are no conflicts to declare.

Acknowledgements

This research was financially supported by São Paulo Research Foundation (FAPESP, grant#2019/00288-0; #2018/16401-8; #2014/50945-4, #2014/50249-8, #2017/10118-0; #2016/19612-4), Coordenação de Aperfeiçoamento de Pessoal de Nível Superior - Brasil (CAPES) – Finance Code 001 and Conselho Nacional de Pesquisa e Desenvolvimento (CNPq, grants no 465571/2014-0, 302874/2017-8 and 427452/2018-0). The authors are also grateful to the Laboratory of Structural Characterization (LCE/DEMa/UFSCar) for helping with the EDS analyses.

Notes and references

1. F. C. Moreira, R. A. R. Boaventura, E. Brillas and V. J. P. Vilar, *Appl Catal B-Environ*, 2017, **202**, 217-261.
2. M. A. Oturan and J.-J. Aaron, *Crit Rev Env Sci Tec*, 2014, **44**, 2577-2641.
3. Z. Ye, D. R. V. Guelfi, G. Álvarez, F. Alcaide, E. Brillas and I. Sirés, *Appl Catal B-Environ*, 2019, **247**, 191-199.
4. Z. Qiang, J.-H. Chang and C.-P. Huang, *Water Res*, 2002, **36**, 85-94.
5. J. Moreira, V. Bocalon Lima, L. Athie Goulart and M. R. V. Lanza, *Appl Catal B-Environ*, 2019, **248**, 95-107.
6. E. Brillas and C. A. Martínez-Huitle, *Appl Catal B-Environ*, 2015, **166-167**, 603-643.
7. M. Panizza and M. A. Oturan, *Electrochim Acta*, 2011, **56**, 7084-7087.
8. G. Coria, T. Pérez, I. Sirés and J. L. Nava, *J Electroanal Chem*, 2015, **757**, 225-229.
9. E. C. Paz, L. R. Aveiro, V. S. Pinheiro, F. M. Souza, V. B. Lima, F. L. Silva, P. Hammer, M. R. V. Lanza and M. C. Santos, *Appl Catal B-Environ*, 2018, **232**, 436-445.
10. Y.-H. Lee, F. Li, K.-H. Chang, C.-C. Hu and T. Ohsaka, *Appl Catal B-Environ*, 2012, **126**, 208-214.
11. P. J. M. Cordeiro-Junior, R. Gonçalves, T. T. Guaraldo, R. da Silva Paiva, E. C. Pereira and M. R. d. V. Lanza, *Carbon*, 2020, **156**, 1-9.
12. H. Zhao, Y. Chen, Q. Peng, Q. Wang and G. Zhao *Appl Catal B-Environ*, 2017, **203**, 127-137.

View Article Online
DOI: 10.1039/D2CP00072E

13. Y. Wang, J. Li and Z. Wei, *J Mater Chem A*, 2018, **6**, 8194-8209.
14. J. M. Gonçalves, M. Ireno da Silva, L. Angnes and K. Araki, *J Mater Chem A*, 2020, **8**, 2171-2206.
15. M. Assumpcao, D. C. Rascio, J. P. B. Ladeia, R. F. B. De Souza, E. T. Neto, M. L. Calegaro, R. T. S. Oliveira, I. Gaubeur, M. R. V. Lanza and M. C. Santos, *Int. J. Electrochem. Sci.*, 2011, **6**, 1586-1596.
16. P. S. Simas, V. S. Antonin, L. S. Parreira, P. Hammer, F. L. Silva, M. S. Kronka, R. B. Valim, M. R. V. Lanza and M. C. Santos, *Electrocatalysis*, 2017, **8**, 311-320.
17. Y. S. Zhang, D. D. Wang, X. L. Wang and F. M. Chen, *J Electroanal Chem*, 2019, **847**, 11.
18. S. Leonard, P. M. Gannett, Y. Rojanasakul, D. Schwegler-Berry, V. Castranova, V. Vallyathan and X. Shi, *J Inorg Biochem*, 1998, **70**, 239-244.
19. Y. Li, Y. Li, B. Xie, J. Han, S. Zhan and Y. Tian, *Environ Sci-Nano*, 2017, **4**, 425-436.
20. B. Cao, G. M. Veith, R. E. Diaz, J. Liu, E. A. Stach, R. R. Adzic and P. G. Khalifah, *Angew Chem Int Edit*, 2013, **52**, 10753-10757.
21. Y. He, Y. Ma, J. Meng, X. Zhang and Y. Xia, *J Catal*, 2019, **373**, 297-305.
22. H. Lv, H. Zhao, T. Cao, L. Qian, Y. Wang and G. Zhao, *J Mol Catal A-Chem*, 2015, **400**, 81-89.
23. L. Liang, Y. An, M. Zhou, F. Yu, M. Liu and G. Ren, *J Environ Chem Eng*, 2016, **4**, 4400-4408.
24. L. Liang, F. Yu, Y. An, M. Liu and M. Zhou, *Environ Sci Pollut R*, 2017, **24**, 1122-1132.
25. H. Zhao, L. Qian, X. Guan, D. Wu and G. Zhao, *Environ Sci Technol*, 2016, **50**, 5225-5233.
26. S. O. Ganiyu, T. X. Huong Le, M. Bechelany, N. Oturan, S. Papirio, G. Esposito, E. van Hullebusch, M. Cretin and M. A. Oturan, *Chem Eng J*, 2018, **350**, 844-855.
27. S. O. Ganiyu, T. X. Huong Le, M. Bechelany, G. Esposito, E. D. van Hullebusch, M. A. Oturan and M. Cretin, *J Mater Chem A*, 2017, **5**, 3655-3666.
28. M. Ghasemi, A. Khataee, P. Gholami, R. D. C. Soltani, A. Hassani and Y. Orooji, *J Environ Manage*, 2020, **267**, 110629.
29. P. Wu, Y. Zhang, Z. Chen, Y. Duan, Y. Lai, Q. Fang, F. Wang and S. Li, *Appl Catal B-Environ*, 2019, **255**, 117784.
30. A. Moraes, M. H. M. T. Assumpção, R. Papai, I. Gaubeur, R. S. Rocha, R. M. Reis, M. L. Calegaro, M. R. V. Lanza and M. C. Santos, *J Electroanal Chem*, 2014, **719**, 127-132.
31. X. Zhang, G. Han, R. Zhang, Z. Huang, H. Shen, P. Su, J. Song and Y. Yang, *ACS Appl Bio Mater*, 2020, **3**, 1469-1480.
32. M. Ghiyasiyan-Arani, M. Masjedi-Arani and M. salavati-Niasari, *J Mol Catal A-Chem*, 2016, **425**, 31-42.
33. W. H. Ji, L. Yin, W. M. Zhu, C. M. N. Kumar, C. Li, H. F. Li, W. T. Jin, S. Nandi, X. Sun, Y. Su, T. Brückel, Y. Lee, B. N. Harmon, L. Ke, Z. W. Ouyang and Y. Xiao, *Phys Rev B*, 2019, **100**, 134420.
34. X. Chu, H. Wang, Y. Chi, C. Wang, L. Lei, W. Zhang and X. Yang, *RSC Adv*, 2018, **8**, 2072-2076.
35. X. Peng, L. Wang, L. Hu, Y. Li, B. Gao, H. Song, C. Huang, X. Zhang, J. Fu, K. Huo and P. K. Chu, *Nano Energy*, 2017, **34**, 1-7.
36. P. Scardi, M. Leoni and K. R. Beyerlein, *Z Krist-Cryst Mater*, 2011, **226**, 924.
37. A. Monshi, M. R. Foroughi and M. R. Monshi, *World J Nano Sci Eng*, 2012, **Vol.02No.03**, 7.
38. H. Jia, J. Stark, L. Q. Zhou, C. Ling, T. Sekito and Z. Markin, *RSC Adv*, 2012, **2**, 10874-10881.
39. G. Xian, N. Zhang, G. M. Zhang, Y. Zhang and Z. G. Zou, *Water Sci. Technol.*, 2019, **79**, 1675-1684.
40. Y. P. Li, Y. F. Yu, Y. F. Huang, R. A. Nielsen, W. A. Goddard, Y. Li and L. Y. Cao, *ACS Catal.*, 2015, **5**, 448-455.
41. D. von Dreifus, R. Pereira, A. D. Rodrigues, E. C. Pereira and A. J. A. de Oliveira, *Ceram Int*, 2018, **44**, 19397-19401.
42. P. Makuła, M. Pacia and W. Macyk, *J Phys Chem Lett*, 2018, **9**, 6814-6817.
43. Y. Xiao, C. Tian, M. Tian, A. Wu, H. Yan, C. Chen, L. Wang, Y. Jiao and H. Fu, *Sci China Mater*, 2018, **61**, 80-90.
44. K. Le, M. Gao, D. Xu, Z. Wang, G. Wang, G. Lu, W. Liu, F. Wang and J. Liu, *Inorg Chem Front*, 2020, **7**, 3646-3656.
45. X. Lv, W. huang, Q. Shi, L. Tang and J. Tang, *J Mater Sci-Mater El*, 2020, **31**, 2388-2397.
46. F. Wu, C. Yu, W. Liu, T. Wang, J. Feng and S. Xiong, *J Mater Chem A*, 2015, **3**, 16728-16736.
47. G. Yang, H. Cui, G. Yang and C. Wang, *ACS Nano*, 2014, **8**, 4474-4487.
48. W. Kwon, J.-M. Kim and S.-W. Rhee, *Electrochim Acta*, 2012, **68**, 110-113.
49. J. T. Han, B. H. Jeong, S. H. Seo, K. C. Roh, S. Kim, S. Choi, J. S. Woo, H. Y. Kim, J. I. Jang, D.-C. Shin, S. Jeong, H. J. Jeong, S. Y. Jeong and G.-W. Lee, *Nat Commun*, 2013, **4**, 2491.
50. S. Shin, V.-D. Dao and H.-S. Choi, *Arab J Chem*, 2020, **13**, 2414-2424.
51. O. Omelianovych, L. L. Larina, H.-J. Oh, E. Park, V.-D. Dao and H.-S. Choi, *Sol Energy*, 2020, **201**, 819-826.
52. T. Q. Nguyen and C. Breitkopf, *J Electrochem Soc*, 2018, **165**, E826-E831.
53. S. Cruz-Manzo, P. Rama and R. Chen, *J Electrochem Soc*, 2010, **157**, B1865.
54. M. T. T. Tran, B. Tribollet, V. Vivier and M. E. Orazem, *Russ J Electrochem+*, 2017, **53**, 932-940.
55. Q. Zhang, M. Zhou, G. Ren, Y. Li, Y. Li and X. Du, *Nat Commun*, 2020, **11**, 1731.
56. S. Dhaka, R. Kumar, M. A. Khan, K.-J. Paeng, M. B. Kurade, S.-J. Kim and B.-H. Jeon, *Chem Eng J*, 2017, **321**, 11-19.
57. E. Baudrin, S. Laruelle, S. Denis, M. Touboul and J. M. Tarascon, *Solid State Ionics*, 1999, **123**, 139-153.